

Infrared Spectroscopy Set

coordinated by

Pierre Richard Dahoo and Azzedine Lakhlifi

Volume 4

**Infrared Spectroscopy of
Symmetric and Spherical
Top Molecules for
Space Observation 2**

Pierre Richard Dahoo
Azzedine Lakhlifi

Color Section

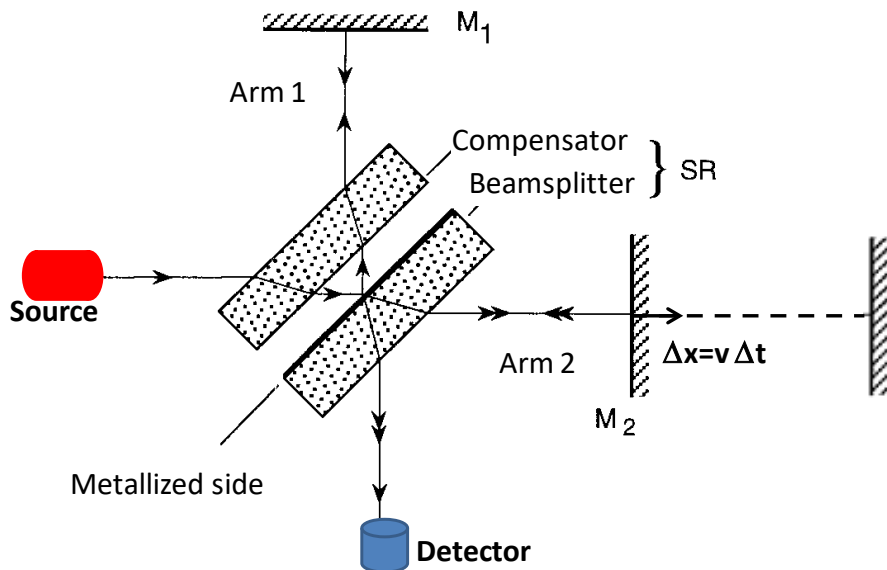


Figure 1.1. Interferometer diagram

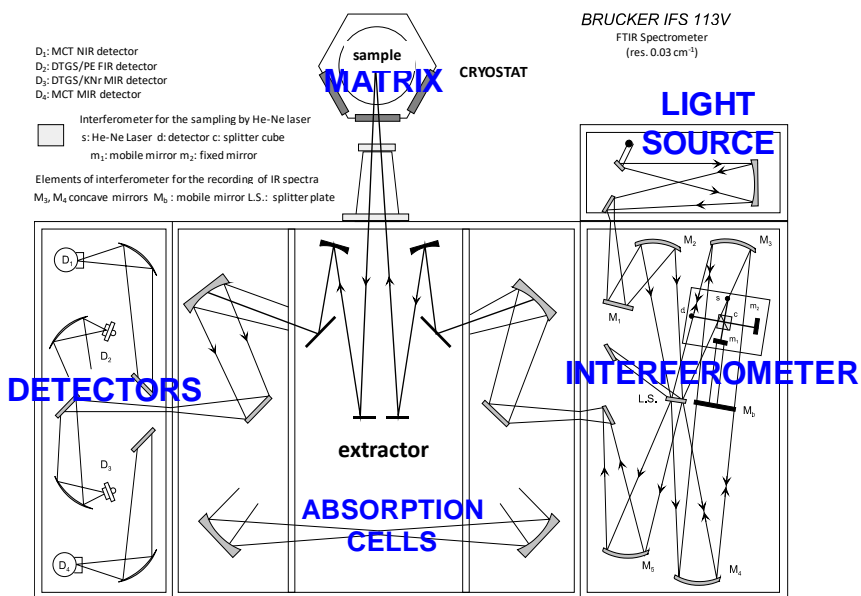


Figure 1.4. FTIR spectrometer and experimental setup

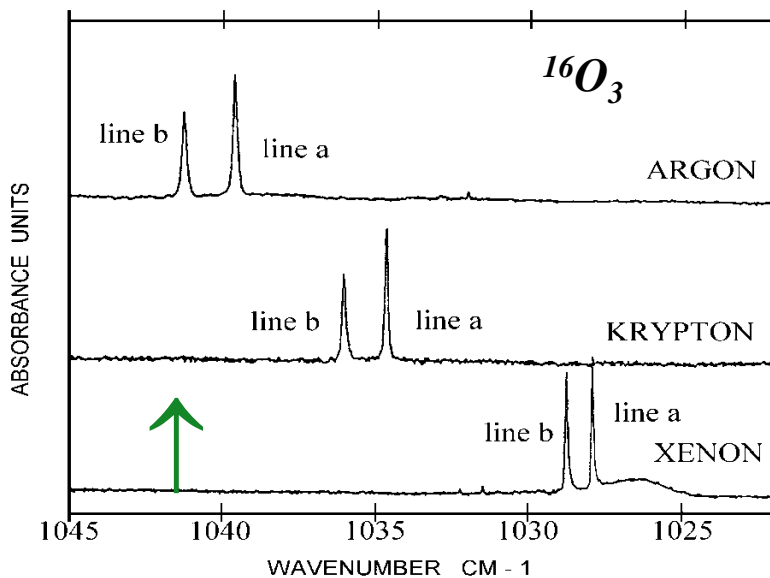


Figure 1.5. O_3 region ν_3 : (a) HF double site and (b) BF simple site (gas: 1042.08 cm^{-1})

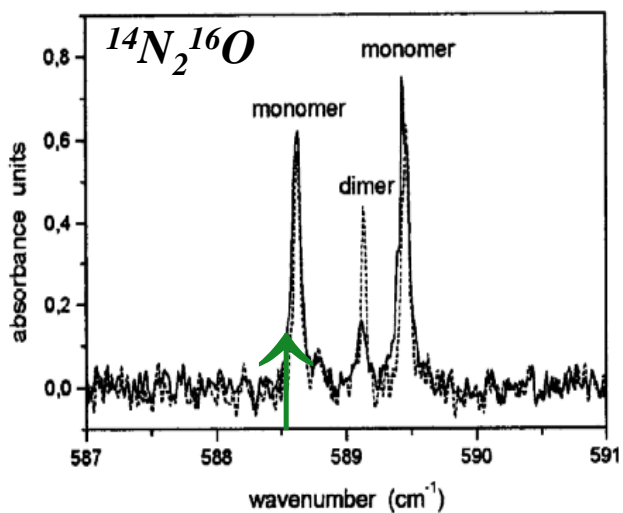


Figure 1.7. N_2O region ν_2 : double site (gas: 588.77 cm^{-1})

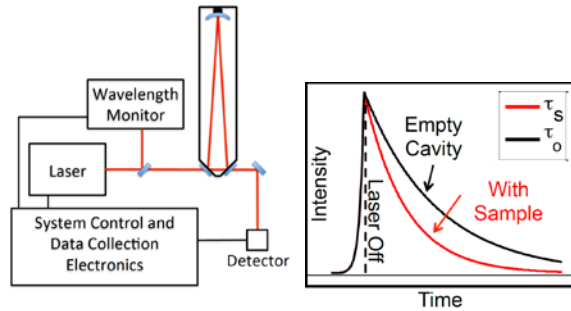


Figure 1.13. Diagram of a CRDS setup and temporal profile of the optical signal in the absence and in the presence of an absorbent

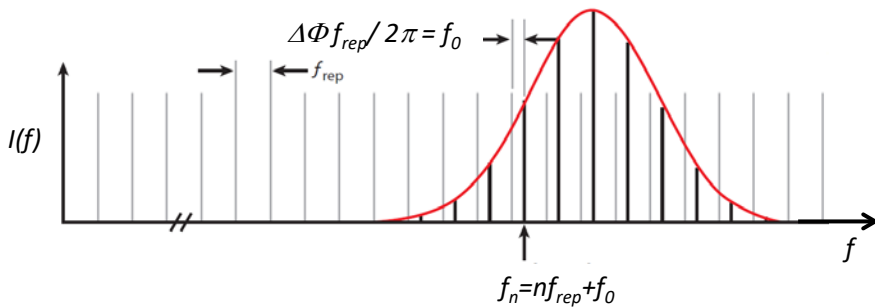


Figure 1.17. Pulse train emitted by a laser source providing a frequency comb in the time domain

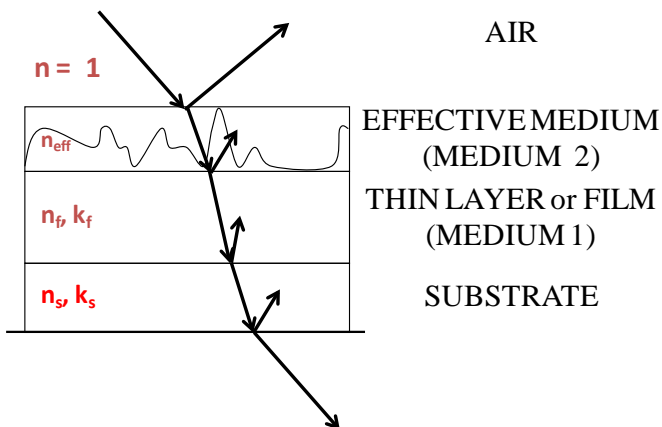


Figure 1.19. Rough surface modeled by an effective medium

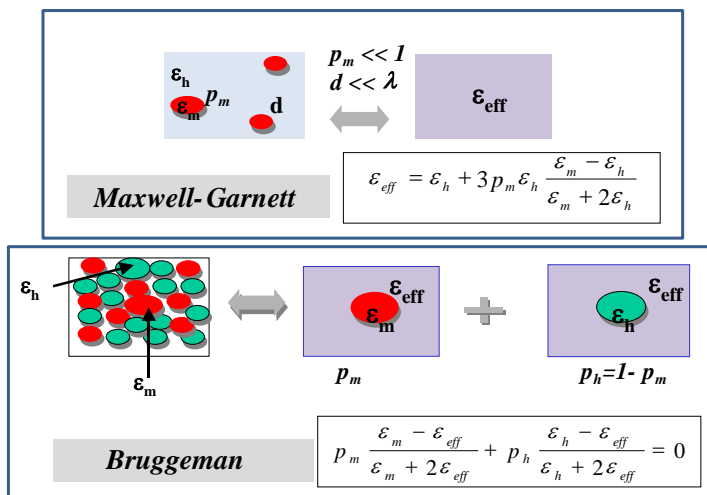


Figure 1.20. Maxwell–Garnett and Bruggeman mean-field models

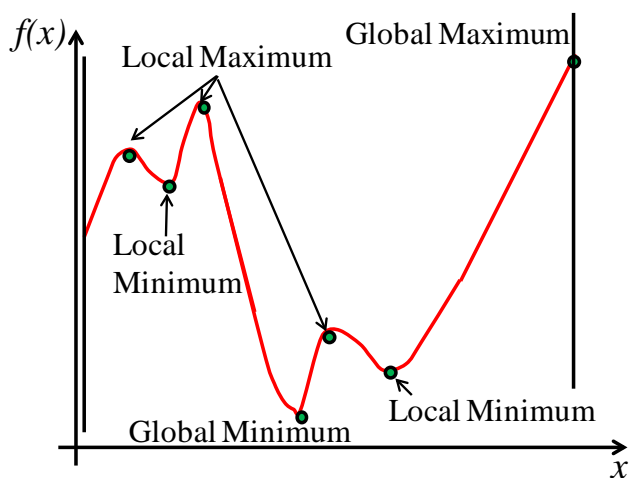


Figure 1.21. Maxima and minima of a function

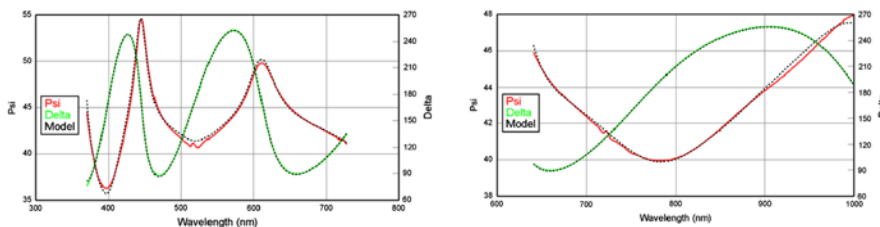


Figure 1.22. Ellipsometric parameters ψ (Psi) and Δ (Delta) on the spectral range of 370–730 nm and 640–1,000 nm and adjustment in the dotted line

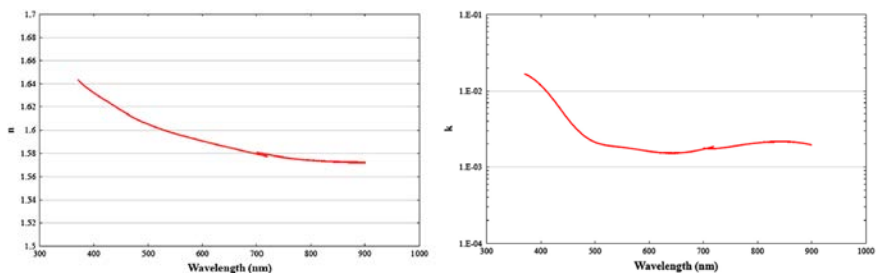


Figure 1.23. Optical constants n and k in the 370–900 nm range

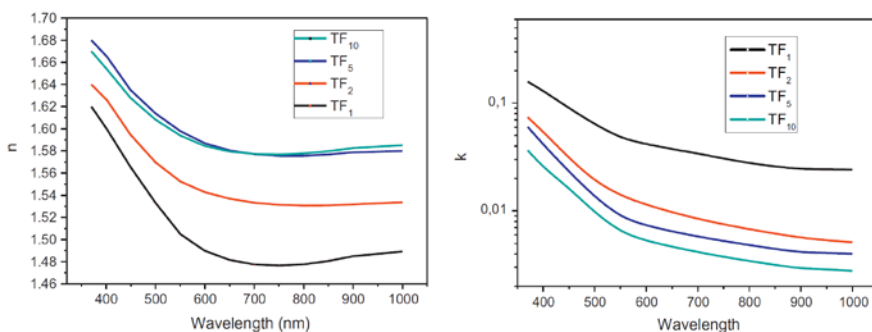


Figure 1.24. Optical constants n and k of tholins between 400 nm and 1,000 nm for various initial concentrations (TF_i : $i\%$) of methane [MAH 12a]

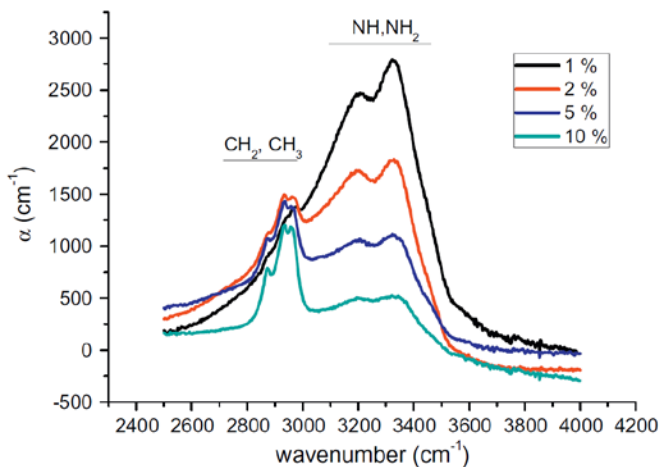


Figure 1.25. Absorption spectra of tholins in mid-infrared for various initial concentrations of CH_4 [MAH 12a]

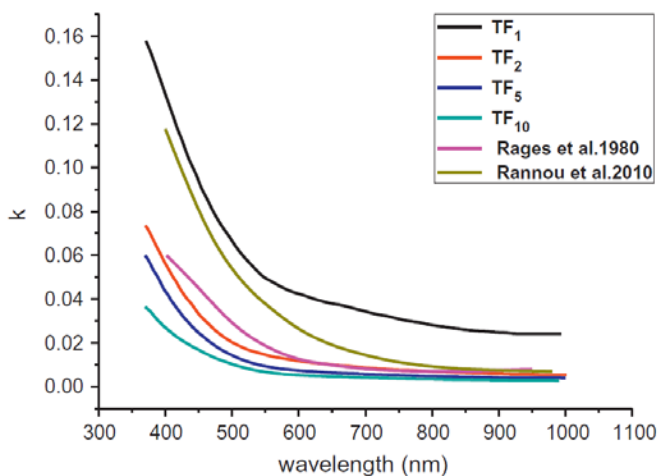


Figure 1.26. Comparison of optical constants k of tholins for various initial concentrations (TF_i : i%) of methane [MAH 12a] and the values deduced from data provided by planetary missions [RAG 80, RAN 10]

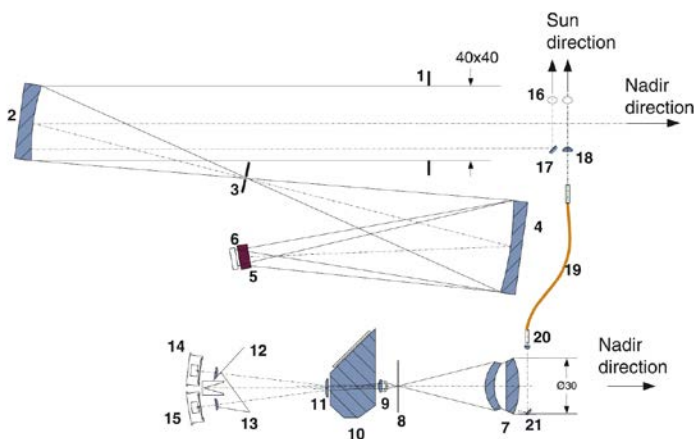


Figure 1.27. Optical diagram of UV and IR channels of SPICAM light. (1) UV channel aperture; (2) off-axis parabolic mirror; (3) slit (mechanically - controlled aperture of variable width from wide to narrow); (4) concave UV grating; (5) intensifier; (6) CCD; (7) IR channel objective; (8) IR FOV diaphragm; (9) and (11) collimation lenses; (10) AOTF crystal; (12) light trap for non-diffracted light; (13) detector proximity lenses; (14) extraordinary beam detector; (15) ordinary beam detector; (16) solar aperture (closed by a shutter when the Sun is not observed); (17) and (21) plane mirror; (18) IR solar entry; (19) optical fiber; (20) fiber collimator [BER 06]

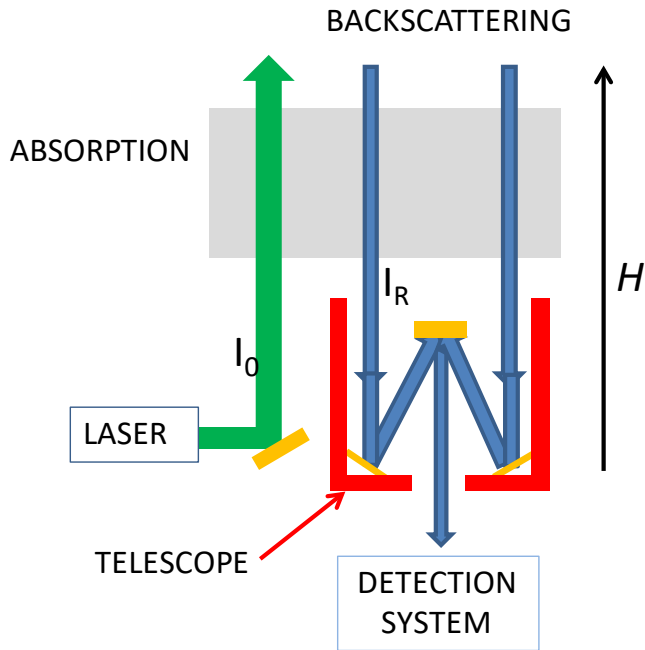


Figure 1.29. *Diagram of the LIDAR operating principle*

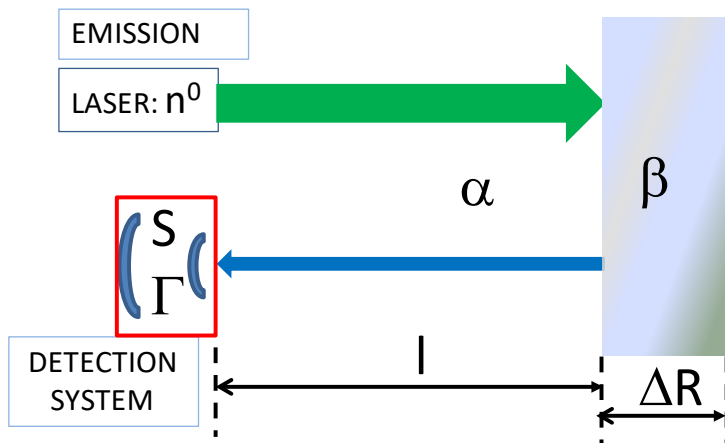


Figure 1.30. *Diagram of LIDAR measurement parameters*

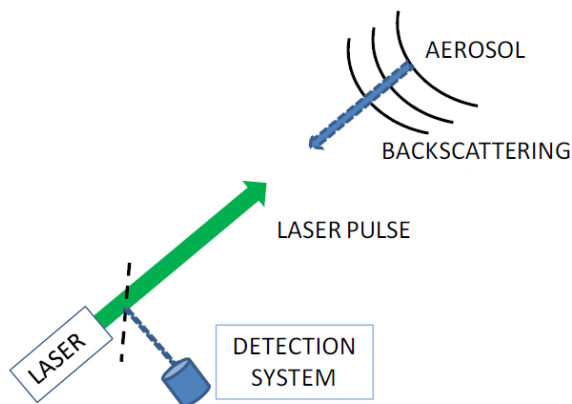


Figure 1.31. *Diagram of the Doppler wind LIDAR observation principle*

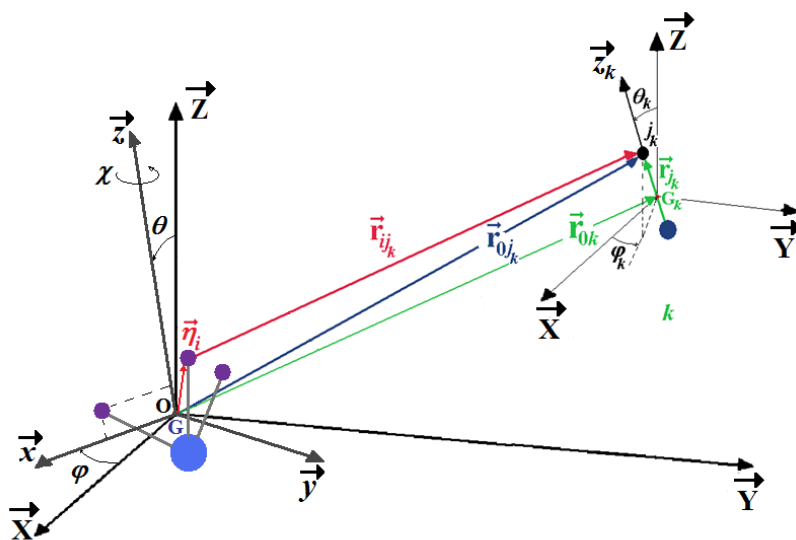


Figure 2.1. *Geometric characteristics of a symmetric top NH_3 molecule in interaction with a (diatomic, for example) molecule of its environment. $(G, \vec{x}, \vec{y}, \vec{z})$ and $(O, \vec{X}, \vec{Y}, \vec{Z})$ are, respectively, the reference frame linked to the equilibrium configuration of the molecule and the fixed reference frame (or laboratory reference frame)*

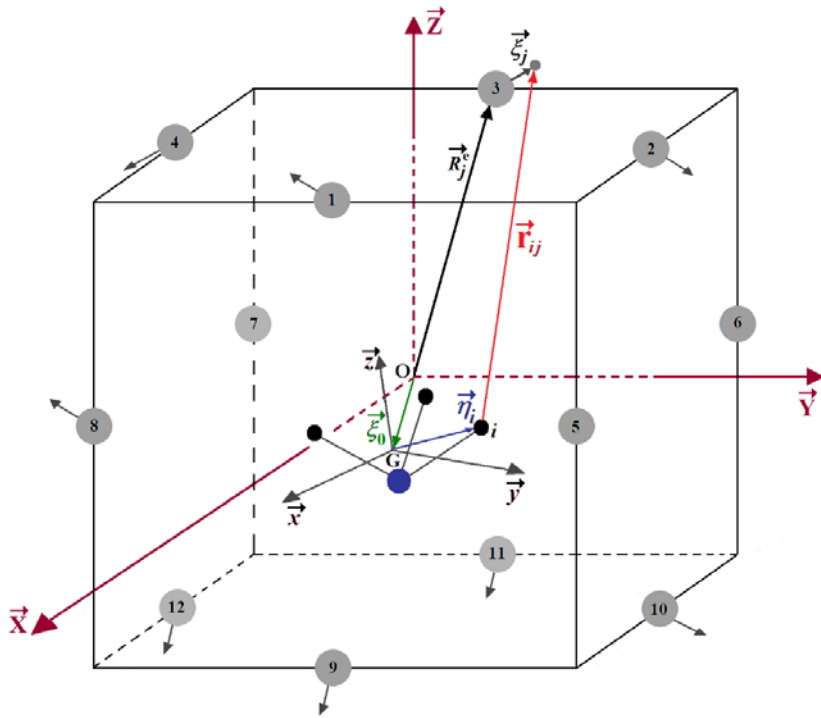


Figure 3.2. Inclusion diagram, in a simple substitution site, of the NH_3 molecule in a rare gas matrix. \vec{R}_j^e is the equilibrium position vector of the atom j in the fixed reference frame $(O, \vec{X}, \vec{Y}, \vec{Z})$ attached to the crystal

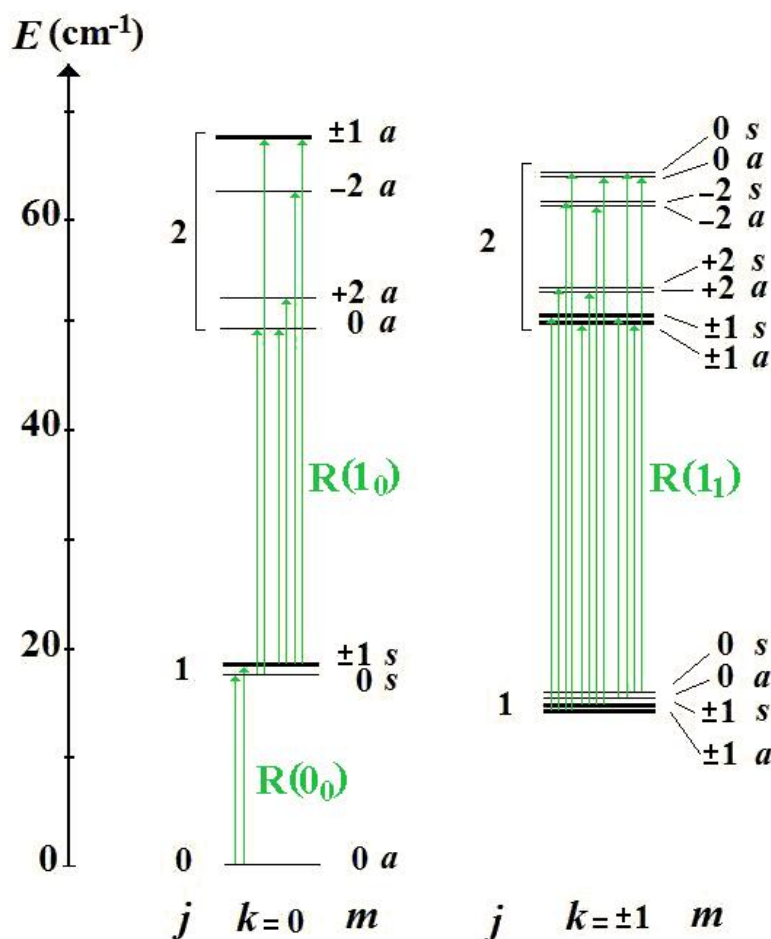


Figure 3.4. Orientational level scheme attached to species A ($k=0$) and E ($k=1$) of NH_3 trapped in an argon matrix, considering the splitting of levels (s for symmetric and a for antisymmetric) due to inversion. The allowed orientational transitions are also presented

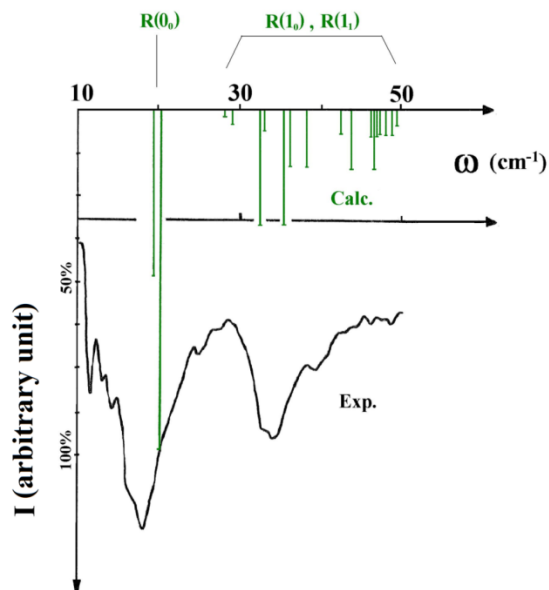


Figure 3.5. Inversion–orientation bar spectrum of NH_3 in an argon matrix calculated at temperature $T = 10$ K and compared to the experimental spectrum obtained by Cugley and Pullin [CUG 72, CUG 73]. The intensity of lines is expressed as the percentage of the most intense line

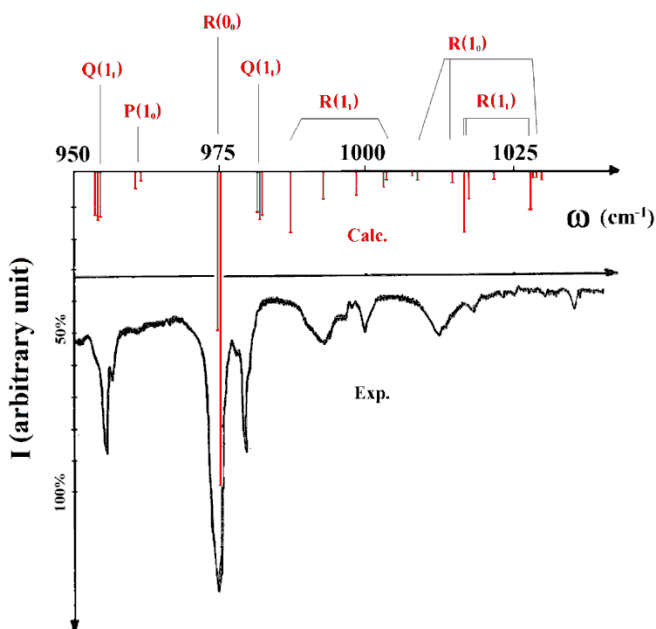


Figure 3.6. Vibration–inversion–orientation bar spectrum of NH_3 in an argon matrix calculated at temperature $T = 10$ K and compared to the experimental spectrum obtained by Abouaf et al. [ABO 77]. The intensity of lines is expressed as the percentage of the most intense line

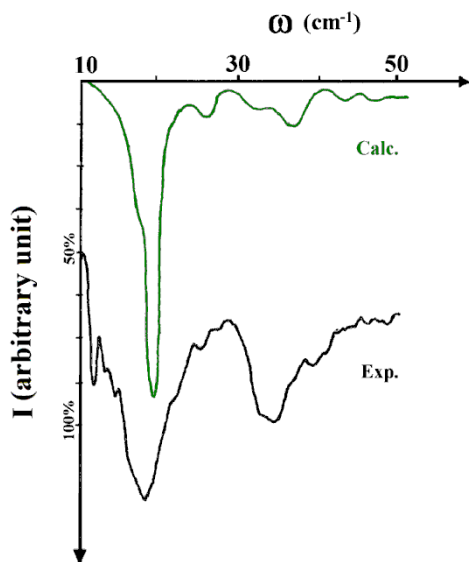


Figure 3.7. *Spectral profile of the inversion–orientation of NH_3 in an argon matrix calculated at $T = 10$ K and compared to the experimental spectrum*

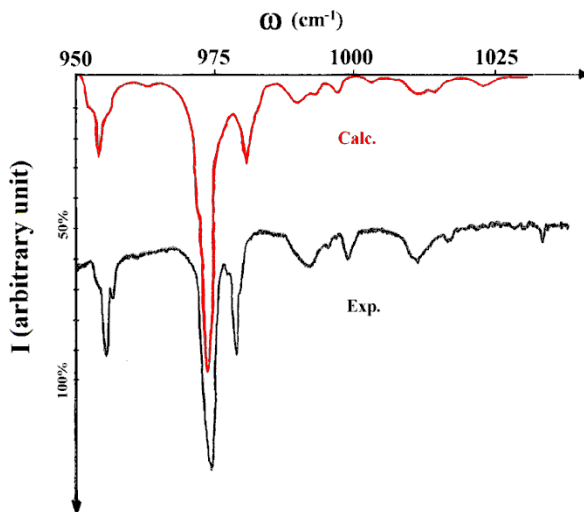


Figure 3.8. *Spectral profile of the vibration–inversion–orientation of NH_3 in an argon matrix calculated at $T = 10$ K and compared to the experimental spectrum*

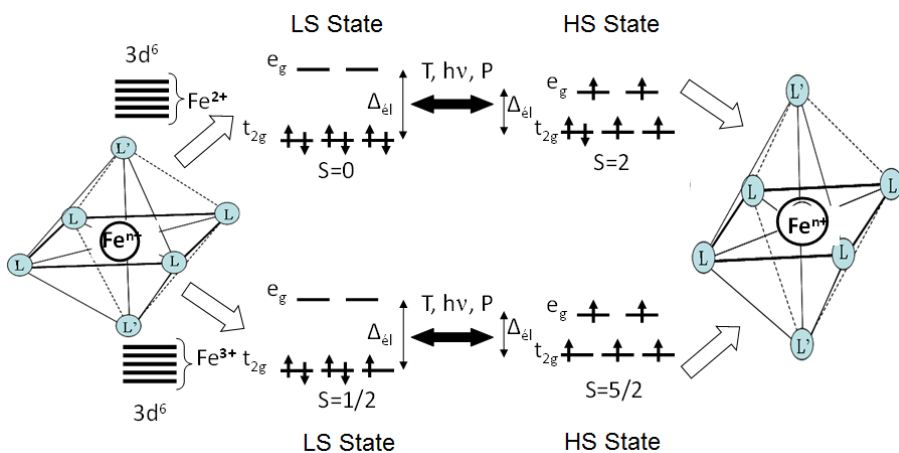


Figure 4.1. LS state and HS state of Fe(II) and Fe(III) ions

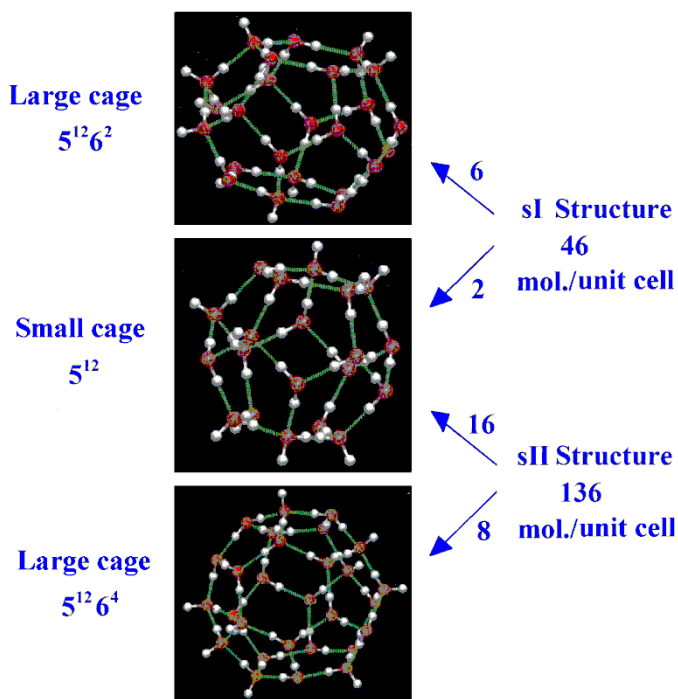


Figure 4.2. Small and large cages forming the sI and sII structures, and the number of water molecules per unit cell

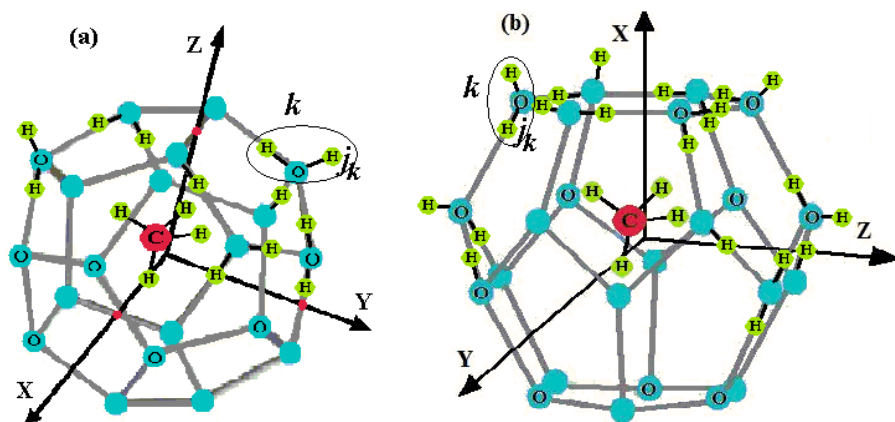


Figure 4.3. Inclusion of a methane (or ammonia) molecule in a small cage (a) and a large cage (b) of the sl structure of clathrate. $(O, \vec{X}, \vec{Y}, \vec{Z})$ is the fixed (laboratory) reference frame attached to the crystal lattice of clathrate

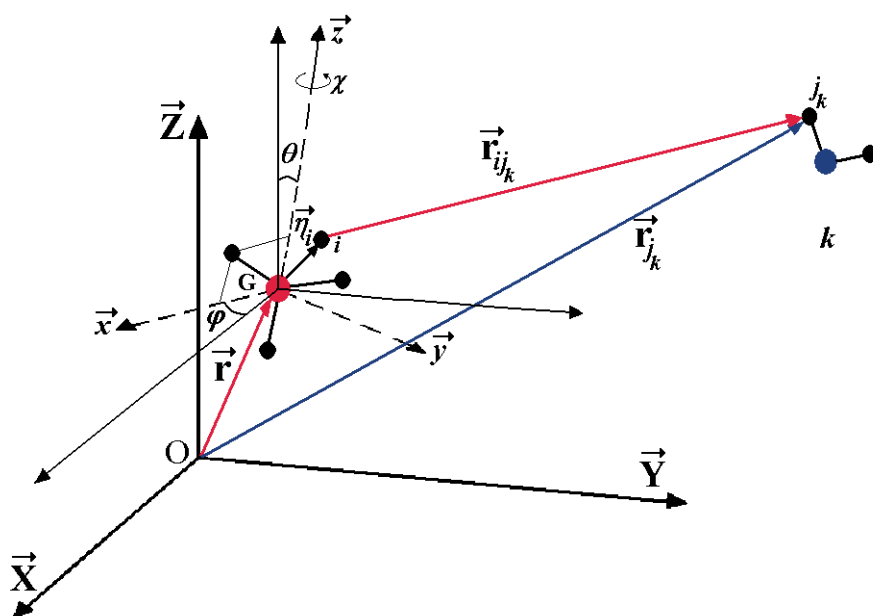


Figure 4.4. Geometric characteristics of a $\text{CH}_4\text{--H}_2\text{O}$ (or $\text{NH}_3\text{--H}_2\text{O}$) pair. The position of the center of mass G and the orientation of the molecule are defined with respect to the fixed reference frame $(O, \vec{X}, \vec{Y}, \vec{Z})$ attached to the clathrate matrix

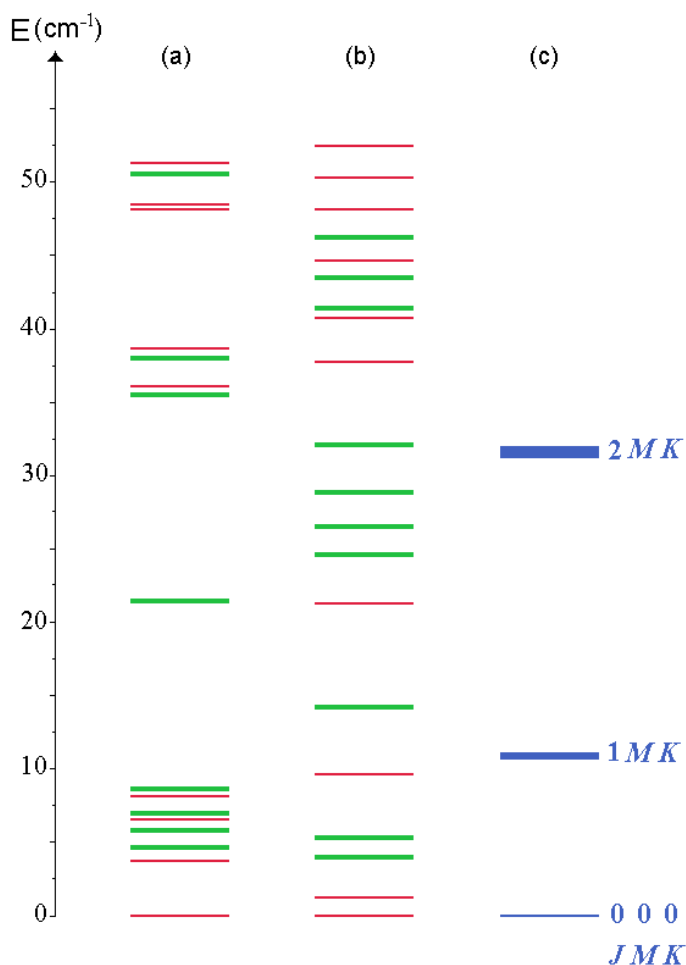


Figure 4.6. Orientational level diagrams of the CH_4 molecule trapped in the clathrate matrix of the *sl* structure: (a) small cage, (b) large cage, and for comparison, (c) the free rotational level diagram of the molecule in the gas phase. The thin lines (red) represent non-degenerate levels and the thick lines represent doubly degenerate levels

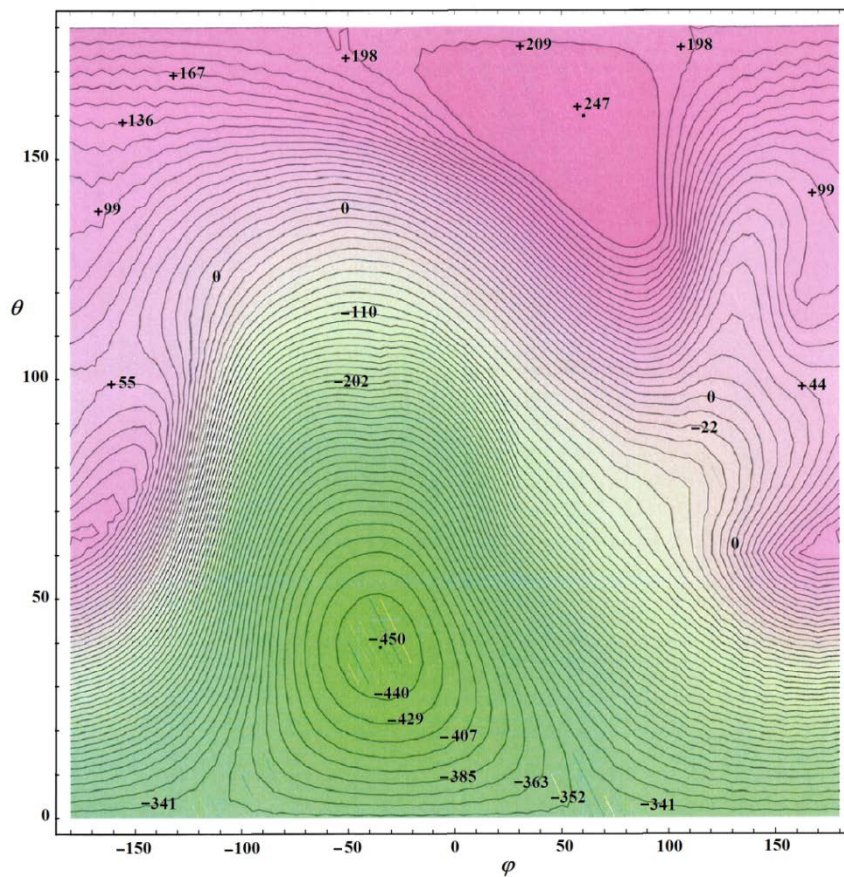


Figure 4.8. Contour maps of the potential energy surface $V_M^{sl-1}(\varphi, \theta)$ (meV) of NH_3 trapped in a large cage of the sl structure

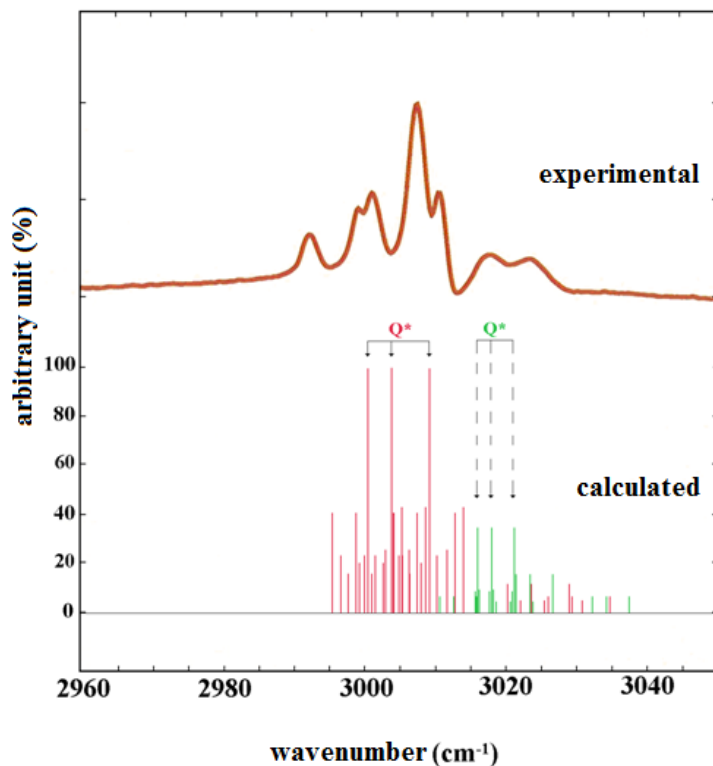


Figure 4.9. Bar spectrum calculated in the vibrational mode ν_3 range of CH_4 trapped in small cages (green lines) and large cages (red lines) of the sl structure

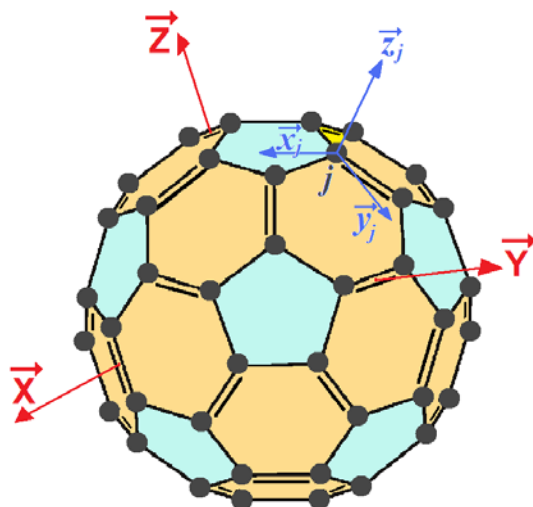


Figure 5.1. Geometry of the fullerene C_{60} molecule. $(O, \bar{X}, \bar{Y}, \bar{Z})$ and $(C_j, \bar{x}_j, \bar{y}_j, \bar{z}_j)$ are, respectively, the fixed (laboratory) reference frame attached to the nanocage and the reference frame attached to the carbon atom C_j

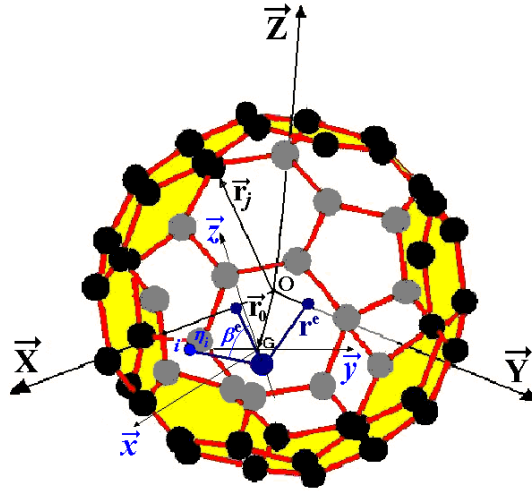


Figure 5.2. Geometric characteristics of a symmetric top NH_3 molecule trapped in a fullerene C_{60} nanocage. $(G, \bar{x}, \bar{y}, \bar{z})$ is the reference frame attached to the equilibrium configuration of the molecule

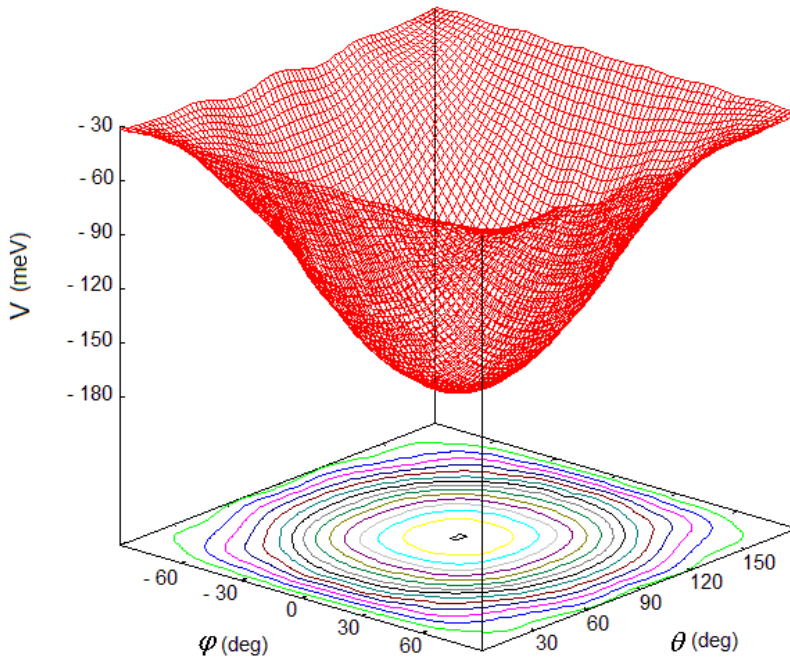


Figure 5.3. Potential energy surface $V_m(\varphi, \theta)$ of the symmetric top NH_3 molecule trapped in a fullerene C_{60} nanocage

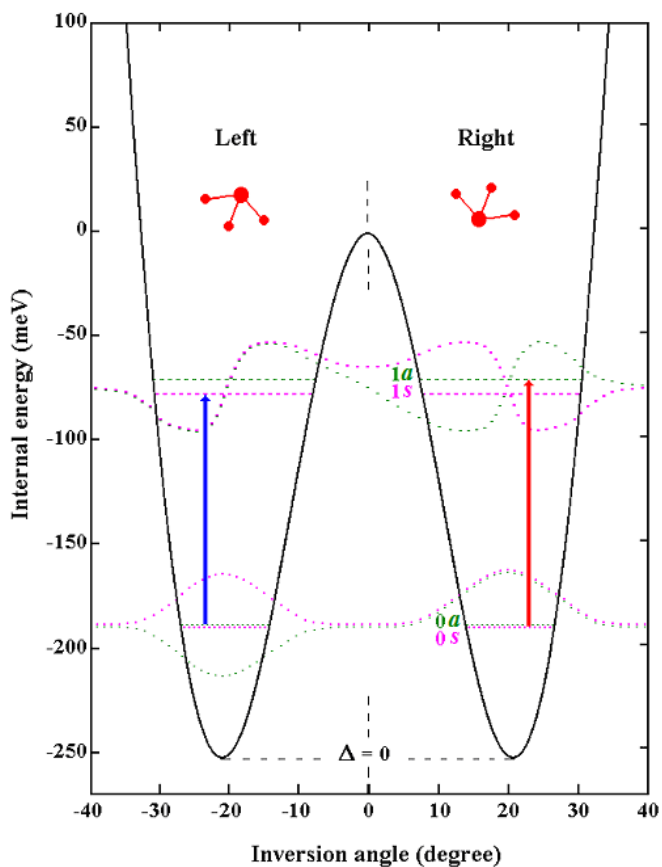


Figure 6.4. Potential energy of the vibration–inversion mode of the NH_3 molecule in the gas phase, depending on the inversion angle, the angle between the N–H bond and the plane formed by the H atoms

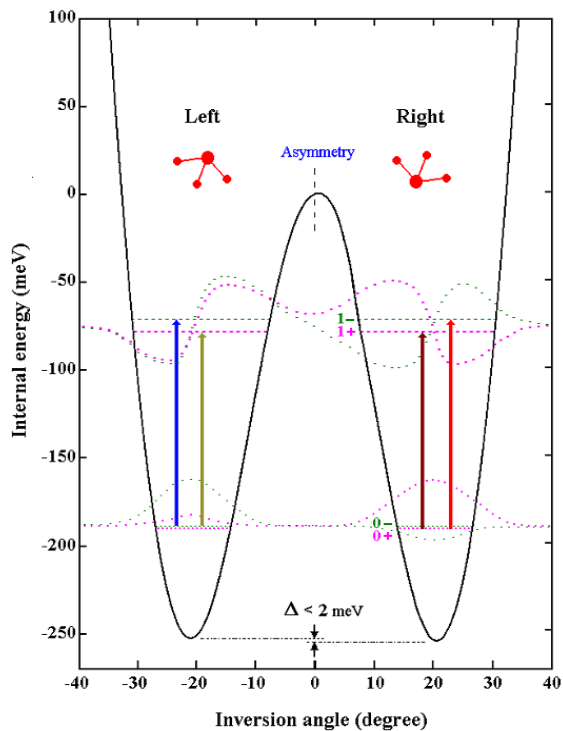


Figure 6.5. Potential energy of the vibration–inversion mode of the NH_3 molecule adsorbed on the graphite surface (1000). Δ represents the energy gap between the potential wells